

mumax⁺: extensible GPU-accelerated micromagnetics and beyond

Lars Moreels^{1†}, Ian Lateur^{1†}, Diego De Gusem^{1†},
Jeroen Mulkers¹, Jonathan Maes¹, Milorad V. Milošević²,
Jonathan Leliaert¹, Bartel Van Waeyenberge¹

¹DyNaMat, Department of Solid State Sciences, Ghent University, 9000
Ghent, Belgium.

²NANOLab Center of Excellence & Department of Physics, University of
Antwerp, 2020 Antwerp, Belgium.

Contributing authors: lars.moreels@ugent.be; ian.lateur@ugent.be;
diego.degusem@ugent.be; milorad.milosevic@uantwerpen.be;
jonathan.leliaert@ugent.be; bartel.vanwaeyenberge@ugent.be;

[†]These authors contributed equally to this work.

Abstract

To address the challenges posed by current magnetism research into systems with complex magnetic ordering and interfaces, we developed mumax⁺, an extensible GPU-accelerated micromagnetic simulator with a Python user interface. It is a general solver for the space- and time-dependent evolution of the magnetization and related vector quantities, using finite difference discretization. Here, we present its design and verification and discuss features not available in mumax³, such as the modeling of antiferromagnets with magnetoelastic coupling. As an illustration of its capabilities, we show that mumax⁺ can predict antiferromagnetic domain walls and their velocity induced by spin transfer torques, as well as the dispersion relations for antiferromagnetic spin waves, elastic waves, and their magnetoelastic anticrossing behavior.

Keywords: antiferromagnetism, dispersion, ferrimagnetism, ferromagnetism, finite difference, GPU, magnetoelasticity, micromagnetism, simulation

1 Introduction

In recent decades, micromagnetic calculations have been a crucial tool for the development of the field of modern magnetism. Especially the availability of open-source [1–7] and GPU-accelerated software packages [5, 8–12] boosted research by enabling efficient numerical studies of nano- and micrometer-sized magnetic systems, complementary to experimental investigations. More recently, research efforts have shifted to more complex magnetic systems such as antiferromagnets [13] and 2D magnetic heterostructures (Van der Waals systems) [14]. Different ways of manipulating the magnetization are being explored as well, e.g. by applying strain [15] and electric field control [16].

In order to model these modern materials, software tools must go beyond the standard micromagnetic theory; preferably, they should be easily extensible to include other physical phenomena of interest. With this in mind, we designed `mumax+`, a versatile GPU-accelerated micromagnetic simulation package. It calculates the space- and time-evolution of nano- to microscale magnets using a finite difference scheme. The program has been designed independently of `mumax3` [5] and features a Python [17] based user interface. This allows users to directly use common packages such as NumPy [18], SciPy [19] and Matplotlib [20] to process and view their data directly. The Python module wraps the main part of the code, which is written in C++ [21] and CUDA [22]. The latter allows calculations to be performed in parallel on a (NVIDIA) GPU, reducing simulation time compared to CPU-based codes. It is also possible to compile the package using double instead of single precision for simulations that require a higher level of precision.

In this paper, we first present the design of the software package with an emphasis on its versatility and extensibility. This is followed by a description of the implemented physics, with the main focus on features not present in `mumax3` [5, 23]. Finally, we demonstrate and verify the capabilities of `mumax+`, which includes the ability to simulate antiferromagnets (and ferrimagnets), with full support for magnetoelastic interactions. We compare simulations of antiferromagnets against theoretical models for the width of domain walls stabilized by interfacial Dzyaloshinskii–Moriya interaction and the velocity of current-driven domain walls. Furthermore, we calculate the dispersion relations of spin waves and magnetoelastic waves in antiferromagnets and demonstrate that `mumax+` obtains the theoretically predicted results.

The development of `mumax+` is motivated by the “plus” mindset, i.e. versatility and extensibility, combined with user-friendliness, in favor of performance and speed. Our intention is not to replace `mumax3`, but rather to offer a platform where additional functionalities can be easily developed and used.

All capabilities of this code have been thoroughly tested against the micromagnetic standard problems [24], `mumax3` [5] and analytical results. These tests will not be repeated here, but can be found freely in the GitHub repository (<https://github.com/mumax/plus>), along with the complete open-source code under the GPLv3 license. Details about dependencies, installation instructions and the API can also be found in the repository.

2 Software design

2.1 Object-orientation

mumax⁺ fully embraces the object-oriented character of C++ and Python. Different magnetic materials can be created and manipulated as individual class instances. Each instance holds on to its own material parameters and has many different quantities which can be evaluated at runtime. Each magnetic instance lives on a user-specified grid within a user-defined world, thereby supporting multiple magnets per world and independent worlds within a script. This is in stark contrast with mumax³, where the magnet coincides with the simulation space and different regions have to be used in order to create different materials or inhomogeneities in material parameters [5]. By adopting the framework of object-oriented programming, mumax⁺ enables this versatility in a clean and user-friendly way.

Internally, mumax⁺ only handles Ferromagnet objects. Antiferromagnets are handled as the set of two such objects, one for each sublattice. Using this two-sublattice model, simulating e.g. ferrimagnets is trivial, since each sublattice can be specified independently. Consequently, all aspects of our discussions here concerning antiferromagnets are equally applicable to ferrimagnets. This modular design allows for the creation of other, more exotic systems.

2.2 Interface

The mumax⁺ module can be imported into a Python input script like any other package. This module contains different classes which can be used to set up a simulation. For example, to create a stack of a ferromagnet and an antiferromagnet, one could use the code snippet below.

```
from mumaxplus import World, Grid, Ferromagnet, Antiferromagnet

world = World(cellsize=(1e-9, 1e-9, 1e-9))
gridsize = (128, 32, 1)
FM = Ferromagnet(world, Grid(gridsize))
AFM = Antiferromagnet(world, Grid(gridsize, origin=(0, 0, 1)))
```

Note that, unlike in mumax³, the origin (0,0,0) of the simulation space is located in the center of the first lower left cell of a magnet grid and can be moved an integer number of cell sizes using the origin parameter, as seen in the code snippet above.

Material parameters can either be set with a scalar value, or with an appropriately shaped NumPy [18] array. NumPy's intuitive array indexing logic makes it easy to create inhomogeneities inside the magnetic material. Alternatively, one can set material parameters using a function which returns a value for each grid coordinate. Consequently, all material parameters can, in principle, have a different value assigned to each grid cell, lifting the restriction of the limited number of regions in mumax³ [5]. These various methods of setting parameters are demonstrated in many of the example scripts in the [GitHub](#) repository.

2.3 Shapes and regions

The magnet geometry can be set using constructive solid geometry [25] to define shapes, just like in mumax³. A wide range of predefined shapes is provided, which can be easily transformed and combined using (Boolean) operators in order to create complex geometries. Alternatively, a geometry can be specified using an array or a function.

Likewise, regions can be defined inside the magnetic material. This provides a user-friendly way to alter the exchange interaction between different (groups of) cells. Since the possibility of setting material parameters using arrays already provides a way to create inhomogeneities, the role of regions is less prominent than in mumax³ [5]. Complementary, Voronoi tessellations are supported in mumax⁺, following mumax³. This provides a convenient way to define multi-grain geometries, e.g. in order to simulate polycrystalline samples. Note that here too, the number of regions is only restricted by the number of grid cells.

3 Implemented physics

3.1 Micromagnetism

For each magnet defined in the simulation world, mumax⁺ solves the dynamic equation

$$\frac{\partial \mathbf{m}}{\partial t} = \boldsymbol{\tau}, \quad (1)$$

where \mathbf{m} is the normalized magnetization, $\boldsymbol{\tau}$ is the sum of the Landau-Lifshitz-Gilbert (LLG) torque and any additional spin-transfer torques as formulated by Zhang and Li [26] or Slonczewski [27], which are implemented in the same way as in mumax³ [5]. The LLG torque is given by

$$\boldsymbol{\tau}_{\text{LLG}} = -\frac{\gamma}{1 + \alpha^2} [\mathbf{m} \times \mathbf{B}_{\text{eff}} + \alpha (\mathbf{m} \times (\mathbf{m} \times \mathbf{B}_{\text{eff}}))], \quad (2)$$

with γ the gyromagnetic ratio and α the dimensionless Gilbert damping constant [28, 29]. When the LLG torque is the only torque present in Eq. (1), one obtains the so-called LLG equation. The different field terms which play a role and add up to the effective field \mathbf{B}_{eff} are calculated based on the current magnetization state $\mathbf{m} \equiv \mathbf{m}(\mathbf{r}, t)$. These fields include an external field, the uniaxial or cubic anisotropy field, the exchange field, a demagnetizing field, stray fields from other magnets, the field induced by the Dzyaloshinskii-Moriya interaction and a thermal field. Of these, the external field, anisotropy fields and thermal field for ferromagnets [30] are implemented in the same way as in mumax³. Their details will not be repeated here, and we refer the interested reader to their detailed description in Ref. [5]. Instead, we shall focus on differences and new features.

3.1.1 Exchange field

The ferromagnetic exchange field is implemented in the same way as in mumax³ [5]. When simulating antiferromagnets or ferrimagnets, this field is extended by two field terms to account for an antiferromagnetic exchange interaction. The total exchange field acting on sublattice s under the influence of the other sublattice s' is described in Ref. [31] and given by

$$\mathbf{B}_{\text{exch}}^{(s)} = \frac{2A_{11}^{(s)}}{M_S^{(s)}} \nabla^2 \mathbf{m}^{(s)} + \frac{A_{12}}{M_S^{(s')}} \nabla^2 \mathbf{m}^{(s')} + \frac{4A_0}{M_S^{(s')} a^2} \mathbf{m}^{(s')}. \quad (3)$$

The first term in Eq. (3) accounts for the standard ferromagnetic exchange interaction. This is the only term present when simulating ferromagnetic systems. The second term contains the inhomogeneous exchange stiffness constant $A_{12} < 0$ J/m and describes a similar antiferromagnetic exchange between sublattices. The last term accounts for the homogeneous exchange interaction between antiferromagnetically coupled spins in the same simulation cell. This term is described by a homogeneous exchange constant $A_0 < 0$ J/m and a lattice parameter a .

3.1.2 Demagnetizing and stray fields

The calculation of the demagnetizing field is entirely based on the work reported in Ref. [32]. At cell i with position \mathbf{r}_i , the field is given by

$$\mathbf{B}(\mathbf{r}_i) = -\mu_0 \sum_{j \neq i} M_S(\mathbf{r}_j) \hat{\mathbf{N}}(\mathbf{r}_i - \mathbf{r}_j) \cdot \mathbf{m}(\mathbf{r}_j), \quad (4)$$

where $M_S(\mathbf{r}_j)$ is the saturation magnetization in cell j , $\hat{\mathbf{N}}(\mathbf{r}_i - \mathbf{r}_j)$ is the symmetric demagnetizing tensor and the sum runs over all cells $j \neq i$ in the grid of the field-generating magnet. The field $\mathbf{B}(\mathbf{r}_i)$ is called the stray field if the cell at \mathbf{r}_i lies outside that magnet. Using the well-known convolution theorem [33], the field equation (Eq. (4)) can be computed by using a fast Fourier transform (FFT) [34]. For antiferromagnets, the magnetization $M_S(\mathbf{r}_j) \mathbf{m}(\mathbf{r}_j)$ is replaced by $M_S^{(1)}(\mathbf{r}_j) \mathbf{m}^{(1)}(\mathbf{r}_j) + M_S^{(2)}(\mathbf{r}_j) \mathbf{m}^{(2)}(\mathbf{r}_j)$, where we account for the possibility of a different saturation magnetization $M_S(\mathbf{r}_j)$ for each sublattice.

The demagnetizing tensor is given by

$$\hat{\mathbf{N}}(\mathbf{r}_i - \mathbf{r}_j) = \frac{1}{4\pi V_i} \int_{S_i} d\mathbf{S} \int_{S'_j} \frac{d\mathbf{S}'}{|\mathbf{r} - \mathbf{r}'|}. \quad (5)$$

The integrals in this equation are taken over the surface of the corresponding cell while V_i is the volume of cell i . The complete analytical derivation of this tensor between any two rectangular blocks (cells) in an array is given in Ref. [32] and the result is used in mumax⁺. This procedure differs from mumax³, where the integrals of the demagnetization tensor in Eq. (5) are computed numerically [5]. The analytical

calculation is more efficient and accurate for small distances of a few cells, whereas numerical integration is more accurate at longer distances [35].

3.1.3 Dzyaloshinskii–Moriya interaction

In `mumax+`, the user can set the individual components of the antisymmetric rank-3 tensor D_{ijk} of the Dzyaloshinskii–Moriya interaction (DMI), which encompasses the DMI strengths and chiral properties of the considered lattice. Convenience methods are provided for common cases where the DMI can be described by a single scalar value (e.g. bulk or interfacial DMI). The corresponding ferromagnetic energy density is defined by

$$\mathcal{E}_{\text{DMI}}^{\text{FM}} = \frac{1}{2} \sum_{i,j,k} D_{ijk} [m_j \partial_i m_k - m_k \partial_i m_j], \quad (6)$$

where the summation runs over spatial indices x , y and z [36, 37]. The structure of Eq. (6) denotes the antisymmetric character of the DMI tensor ($D_{ijk} = -D_{ikj}$), meaning it can be described using 9 independent parameters. The tensorial character of the DMI also comes into play when calculating the Neumann boundary conditions, which for ferromagnets are implemented as [36]

$$2A_{11} \partial_{\mathbf{n}} \mathbf{m} = \mathbf{\Gamma}, \quad \text{where} \quad \Gamma_k = \sum_{i,j} m_j n_i D_{ijk}, \quad (7)$$

and \mathbf{n} is the surface normal.

Since the DMI tensor is determined by the crystallographic and magnetic symmetries of the material, each antiferromagnetic sublattice can have its own tensor. Furthermore, a third DMI tensor is used to describe the intersublattice interaction. Generally, the energy density due to DMI in an antiferromagnet can be written as [37]

$$\mathcal{E}_{\text{DMI}}^{\text{AFM}} = \sum_{s,s'} \sum_{i,j,k} D_{ijk}^{(s,s')} m_j^{(s)} \partial_i m_k^{(s')}, \quad (8)$$

where the indices s and s' denote the different sublattices. It is assumed that $D_{ijk}^{(s,s')} = D_{ijk}^{(s',s)}$, meaning there can be up to three tensors to describe the full DMI in an antiferromagnet.

The Neumann boundary conditions in Eq. (7) are extended in the antiferromagnetic case to take both sublattices into account. Given the structure of the exchange field in Eq. (3), the boundary conditions for a sublattice s in an antiferromagnet are given by [31, 36]

$$2A_{11}^{(s)} \partial_{\mathbf{n}} \mathbf{m}^{(s)} = A_{12} \left(\partial_{\mathbf{n}} \mathbf{m}^{(s')} \times \mathbf{m}^{(s)} \right) \times \mathbf{m}^{(s)} + \mathbf{\Gamma}^{(s)}, \quad (9)$$

where an extra term proportional to the inhomogeneous exchange constant A_{12} takes the interaction with the other sublattice into account. The term $\Gamma^{(s)}$ is calculated as in Eq. (7).

The Neumann boundary conditions as given in Eqs. (7) and (9) are the default in `mumax+`. Alternatively, open or periodic boundary conditions can be used. In general, the chosen boundary conditions will not only affect the DMI field calculations, but also the ferromagnetic and antiferromagnetic inhomogeneous exchange calculations. Periodic boundary conditions also affect the calculation of demagnetizing and stray fields.

3.1.4 Thermal fields in antiferromagnets

The thermal field in antiferromagnets is implemented with each sublattice having its own thermal field, as if it were an independent ferromagnetic lattice, as is done in Boris [10]. To validate this approach, one can consider a thought experiment with two sublattices with uniaxial anisotropy, a positive homogeneous exchange coupling between them and no demagnetizing field. The anisotropy results in two energy minima, with uniform magnetization, separated by an energy barrier. The spins can switch from one minimum to the other under the influence of a thermal field. The analytical expression of this switching rate for the case of ferromagnets is well-known [5, 38]. In the limit of low exchange coupling, each sublattice is expected to have the same switching time as a ferromagnet with the same saturation magnetization and anisotropy as either sublattice, since each sublattice acts independently as a single ferromagnetic lattice. In the limit of high coupling, the sublattice moments within a simulation cell must behave collectively, effectively doubling the magnetic moment. To keep the anisotropic energy per moment constant, the anisotropy constant would have to be doubled as well. We simulate an ensemble of spins with uniaxial anisotropy at 400 K for a range of coupling constants using `mumax+`, the results of which are shown in Fig. 1. In the limit of low exchange coupling, the sublattices behave as a ferromagnet with the same M_S and K_{u1} . In the limit of high coupling, the datapoints coincide with the switching time of a ferromagnet with $2M_S$ and $2K_{u1}$, confirming the validity of this approach.

3.2 Elasticity

Apart from the magnetodynamic equation (Eq. (1)), `mumax+` can also solve the second order elastodynamic equation [39, 40]

$$\rho \frac{\partial^2 \mathbf{u}}{\partial t^2} = \mathbf{f}_{\text{tot}}, \quad (10)$$

or, equivalently, the two first order differential equations

$$\begin{aligned} \frac{\partial \mathbf{u}}{\partial t} &= \mathbf{v} \\ \frac{\partial \mathbf{v}}{\partial t} &= \mathbf{a} = \frac{\mathbf{f}_{\text{tot}}}{\rho}, \end{aligned} \quad (11)$$

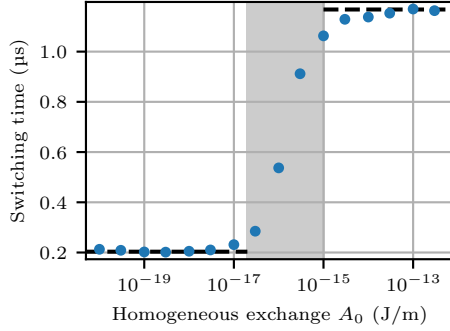


Fig. 1: Datapoints show the simulated switching times as a function of the homogeneous coupling constant A_0 between two sublattices with a saturation magnetization of $M_S = 400$ kA/m and a uniaxial anisotropy constant $K_{u1} = 2.5$ kJ/m³. The left dashed line shows simulated results of the switching time of a ferromagnet with the same M_S and K_{u1} as each individual sublattice, while the right line shows results for a ferromagnet with $2M_S$ and $2K_{u1}$. All simulations were performed at 400 K.

with \mathbf{u} the elastic displacement, \mathbf{v} the velocity, \mathbf{a} the acceleration, ρ the mass density and the total body force density $\mathbf{f}_{\text{tot}} = \mathbf{f}_d + \mathbf{f}_{\text{ext}} + \mathbf{f}_{\text{el}}$. The latter contains a damping force $\mathbf{f}_d = -\eta \mathbf{v}$ with a phenomenological damping parameter η , an external force \mathbf{f}_{ext} set by the user, and the elastic body force $\mathbf{f}_{\text{el}} = \nabla \cdot \hat{\sigma}$. The second order mechanical stress tensor $\hat{\sigma}$ is given by Hooke's law $\hat{\sigma} = \hat{\mathbf{c}} : \hat{\varepsilon}$, where $\hat{\mathbf{c}}$ is the fourth order stiffness tensor and $\hat{\varepsilon} = \frac{1}{2} (\nabla \mathbf{u} + (\nabla \mathbf{u})^T)$ is the symmetric second order strain tensor. The material is assumed to have a cubic crystal structure, so in reduced dimensionality (Voigt notation) $\hat{\mathbf{c}}$ can be fully described by three components: C_{11} , C_{12} and C_{44} [41].

The implementation is mostly based on a previous extension of `mumax3` [42], except that the elastic force \mathbf{f}_{el} does not use second order differences of the elastic displacement. Rather, the elastic force \mathbf{f}_{el} is computed as the numeric divergence of the stress, while the strain is calculated with the numeric gradient of the displacement. In this way, traction-free boundary conditions [43] were easily implemented. These impose $\hat{\sigma} \cdot \mathbf{n} = \mathbf{0}$ at the boundary, where \mathbf{n} is the normal to the boundary. The accuracy is also higher, as both spatial derivative calculations utilize a fourth order accurate central difference scheme [44] in the bulk material. Lower order schemes are used close to and at the boundaries.

3.3 Magnetoelasticity

Magnetoelasticity for ferromagnets is implemented in the same way as described in Ref. [42]. It is the combination of magnetostriction [45], where the magnetization affects the elastic displacement, and the Villari effect or inverse magnetostriction [45], where the elastic strain affects the magnetization. For materials with cubic crystal

symmetry, the first effect is described by a body force density

$$\mathbf{f}_{\text{mel}} = 2B_1 \begin{bmatrix} m_x \partial_x m_x \\ m_y \partial_y m_y \\ m_z \partial_z m_z \end{bmatrix} + B_2 \begin{bmatrix} m_x (\partial_y m_y + \partial_z m_z) + m_y \partial_y m_x + m_z \partial_z m_x \\ m_y (\partial_x m_x + \partial_z m_z) + m_x \partial_x m_y + m_z \partial_z m_y \\ m_z (\partial_x m_x + \partial_y m_y) + m_x \partial_x m_z + m_y \partial_y m_z \end{bmatrix}, \quad (12)$$

which is added to \mathbf{f}_{tot} in Eq. (11). The constants B_1 and B_2 are the first and second magnetoelastic coupling constants. The second effect adds a magnetoelastic field \mathbf{B}_{mel} to the effective field \mathbf{B}_{eff} in Eq. (2):

$$\mathbf{B}_{\text{mel}} = -\frac{2}{M_S} \left(B_1 \begin{bmatrix} \varepsilon_{xx} m_x \\ \varepsilon_{yy} m_y \\ \varepsilon_{zz} m_z \end{bmatrix} + B_2 \begin{bmatrix} \varepsilon_{xy} m_y + \varepsilon_{xz} m_z \\ \varepsilon_{xy} m_x + \varepsilon_{yz} m_z \\ \varepsilon_{xz} m_x + \varepsilon_{yz} m_y \end{bmatrix} \right), \quad (13)$$

where ε_{ij} ($i, j = x, y, z$) are the components of the strain tensor $\hat{\varepsilon}$.

Magnetoelasticity for antiferromagnets and ferrimagnets is implemented similarly to how it is reported in Ref. [46]. The whole magnet has a shared elastic displacement, velocity, stiffness and body force, while each ferromagnetic sublattice s has its own magnetoelastic coupling constants $B_1^{(s)}$ and $B_2^{(s)}$ and uses its own magnetization $\mathbf{m}^{(s)}$ and saturation magnetization $M_S^{(s)}$. Each sublattice then creates a magnetoelastic body force $\mathbf{f}_{\text{mel}}^{(s)}$, which is added to the total body force \mathbf{f}_{tot} in Eq. (11). Conversely, each sublattice magnetization is affected by a unique magnetoelastic field $\mathbf{B}_{\text{mel}}^{(s)}$ created by its own magnetization $\mathbf{m}^{(s)}$ and the shared strain $\hat{\varepsilon}$.

3.4 Time integration

For the numerical time integration of the dynamical equations, the timesolver in `mumax+` can utilize several embedded Runge-Kutta methods with the option to use adaptive time stepping [47–51]. In Tab. 1 we show the available methods with their convergence order and the order of the error estimate, which is used for adaptive time stepping. The Fehlberg method is the default solver in `mumax+` and all methods are implemented by using their Butcher tableau, making it easy to add more.

Table 1: Runge-Kutta solvers in `mumax+` together with their convergence order and error estimate order which is used for adaptive time stepping.

Method	Convergence order	Error estimate order
Heun (RK12)	2	1
Bogacki-Shampine (RK23)	3	2
Cash-Karp	5	4
Fehlberg (RKF45)	5	4
Dormand-Prince (RK45)	5	4

Besides the standard time integration, mumax⁺ also provides a minimize [52] and relax function to find the system’s energy minimum. The implementation of both is similar to mumax³ [5]. In order to find the energy minimum of an antiferromagnet, the algorithms consider both sublattices and their energy is minimized simultaneously.

4 Verification

The mumax⁺ software was thoroughly tested with the different micromagnetic standard problems [24] and analytical results, and by comparing it with results obtained with mumax³. These tests can be found in the GitHub repository and can be run using pytest [53]. Since the implementation of antiferromagnets and elastodynamics extends beyond the physics included in mumax³, the remainder of this section will treat the verification of these two features.

4.1 Width and velocity of an antiferromagnetic domain wall stabilized by interfacial DMI

In Ref. [31] it is shown that an antiferromagnetic domain wall can be stabilized by interfacial DMI in a thin film antiferromagnet with uniaxial out-of-plane anisotropy. The authors give an analytical derivation of the static domain wall width, which results in

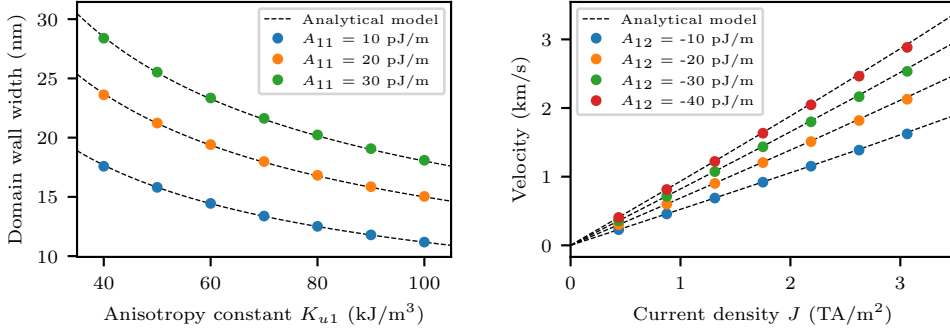
$$\Delta = \sqrt{\frac{2A_{11} - A_{12}}{2K_{u1}}}, \quad (14)$$

where K_{u1} is the uniaxial anisotropy constant and the different exchange constants are defined in Eq. (3). We compare this result with simulations performed with mumax⁺. Fig. 2a shows the domain wall width in the same system as considered in Ref. [31] for different material parameters. The results from mumax⁺ agree well with the analytical result of Eq. (14). This validates the implementation of both the different exchange terms and the DMI in antiferromagnetic systems.

The system can be investigated further by applying a current to the antiferromagnetic thin film. An analytical expression for the domain wall velocity is derived in Ref. [31] and given by

$$v = \frac{\pi\gamma\hbar}{8e} \cdot \frac{PJ}{t\alpha M_S} \left(\cos\Phi^{(1)} - \cos\Phi^{(2)} \right) \cdot \Delta(J), \quad (15)$$

where \hbar , e , t , P and J are the reduced Planck’s constant, elementary charge, film thickness, current polarization and applied current density respectively. The angle $\Phi^{(s)}$ denotes the angle between the sublattice magnetization $\mathbf{m}^{(s)}$ and the x -axis along the length of the film ($s = 1, 2$). As derived in Ref. [31], the domain wall width $\Delta \equiv \Delta(J)$ contracts under the application of a current, rendering a different expression than the one in Eq. (14). Fig. 2b shows results of the simulation of the domain wall velocity under different applied current densities. These results correspond well with Eq. (15).



(a) Data points show domain wall widths for varying uniaxial anisotropy and inhomogeneous ferromagnetic exchange constants, K_{u1} and A_{11} respectively. The antiferromagnetic homogeneous and inhomogeneous exchange coupling constants $A_0 = -25 \text{ pJ/m}$ and $A_{12} = -5 \text{ pJ/m}$ are held fixed.

(b) Data points show domain wall velocities for different applied current densities J and inhomogeneous antiferromagnetic exchange constant A_{12} . The polarization $P = 0.044$, Λ -parameter $\Lambda = 1$ [5], uniaxial anisotropy constant $K_{u1} = 64 \text{ kJ/m}^3$ and different exchange constants $A_{11} = 2 \text{ pJ/m}$ and $A_0 = -2 \text{ pJ/m}$ are held fixed.

Fig. 2: Figures show static domain wall widths (a) and domain wall velocities (b) in an antiferromagnetic thin-film consisting of $200 \times 100 \times 1$ cubic cells with a length of 2 nm. The sublattices have a saturation magnetization of 0.4 MA/m and the domain wall is stabilized by an interfacial DMI with a strength of 0.11 mJ/m². The results correspond well to the analytical description shown in Eqs. (14) and (15) for the domain wall width and velocity respectively.

4.2 Spin waves in antiferromagnets

The dispersion relation for spin waves in ferromagnets has been calculated in Refs. [54–56]. The method presented there can be extended to antiferromagnets, by considering two coupled LLG equations describing the exchange-coupled sublattices (Eqs. (1)–(3)). We consider a collinear antiferromagnet with uniaxial anisotropy K_{u1} along the z -axis and an external field \mathbf{B}_{ext} in the z -direction. The demagnetizing field is assumed to be negligible due to the collinearity. The unperturbed magnetization lies along the z -direction and we apply a perturbation in the x - and y -directions. The resulting magnetization of the sublattices is then given by

$$\mathbf{m}^{(1)} = \begin{bmatrix} 0 \\ 0 \\ 1 \end{bmatrix} + \begin{bmatrix} m_x^{(1)} \\ m_y^{(1)} \\ 0 \end{bmatrix} e^{i(\omega t + \mathbf{k} \cdot \mathbf{r})}, \quad \text{where} \quad \mathbf{m}^{(2)} = \begin{bmatrix} 0 \\ 0 \\ -1 \end{bmatrix} + \begin{bmatrix} m_x^{(2)} \\ m_y^{(2)} \\ 0 \end{bmatrix} e^{i(\omega t + \mathbf{k} \cdot \mathbf{r})}. \quad (16)$$

The dispersion relation can now be obtained by calculating each component of the LLG equation up to the first order in the perturbation for both sublattices. The result

is a set of four equations given by

$$\begin{aligned}
i\omega m_x^{(1)} + (\omega_{\text{ext}} + \omega_{\text{ani}} - \omega_0 + \omega_{11}) m_y^{(1)} - (\omega_0 - \omega_{12}) m_y^{(2)} &= 0, \\
i\omega m_y^{(1)} - (\omega_{\text{ext}} + \omega_{\text{ani}} - \omega_0 + \omega_{11}) m_x^{(1)} + (\omega_0 - \omega_{12}) m_x^{(2)} &= 0, \\
i\omega m_x^{(2)} + (\omega_{\text{ext}} - \omega_{\text{ani}} + \omega_0 - \omega_{11}) m_y^{(2)} + (\omega_0 - \omega_{12}) m_y^{(1)} &= 0, \\
i\omega m_y^{(2)} - (\omega_{\text{ext}} - \omega_{\text{ani}} + \omega_0 - \omega_{11}) m_x^{(2)} - (\omega_0 - \omega_{12}) m_x^{(1)} &= 0.
\end{aligned} \tag{17}$$

Here we defined

$$\begin{aligned}
\omega_{\text{ext}} &= \gamma B_{\text{ext}}, & \omega_{\text{ani}} &= \gamma \frac{2K_{u1}}{M_S}, & \omega_0 &= \gamma \frac{4A_0}{a^2 M_S}, \\
\omega_{11} &= \gamma \frac{2A_{11}}{M_S} k^2, & \omega_{12} &= \gamma \frac{A_{12}}{M_S} k^2,
\end{aligned}$$

where M_S , K_{u1} and A_{11} are identical for both sublattices. Notice that there are no equations for the z -component of the LLG equations, as these only contain terms of second order in the perturbation. Physically nontrivial solutions of the set of equations (17) exist when the associated 4×4 matrix representation becomes singular, occurring when its determinant equals zero. This condition yields the four dispersion relations for a bulk antiferromagnet:

$$\omega = \pm \sqrt{(\omega_{\text{ani}} + \omega_{11} - \omega_{12})(\omega_{\text{ani}} + \omega_{11} - 2\omega_0 + \omega_{12})} \pm \omega_{\text{ext}}. \tag{18}$$

The anisotropy creates a frequency gap, while the external field lifts the frequency degeneracy. In absence of anisotropy, $\omega_{\text{ani}} = 0$ THz/rad, the dispersion relation becomes characteristically linear [57–59] for small values of the wave number k .

$$\omega \approx \pm \frac{\gamma}{M_S} \sqrt{-8 \frac{A_0}{a^2} (2A_{11} - A_{12}) |k|} \pm \omega_{\text{ext}}, \quad k \ll \sqrt{\frac{-8A_0/a^2}{2A_{11} + A_{12}}} \tag{19}$$

To check if mumax⁺ recovers the same dispersion relation, we ran a simulation of a one-dimensional wire containing 2560 cubic cells with a length of 0.5 nm and a lattice parameter a of 0.35 nm. The magnet has a saturation magnetization of 400 kA/m and exchange parameters $A_{11} = 10$ pJ/m, $A_0 = -400$ pJ/m and $A_{12} = -5$ pJ/m. The uniaxial anisotropy constant has a value of 1 kJ/m³ and the external field has a strength of 0.4 T. The simulation ran for 2 ps, during which a magnetic field sinc pulse was applied in the wire direction. A temporal and spatial Fourier transform of the magnetization of one of the sublattices was then performed and the result is shown in Fig. 3. It shows a good agreement with the theoretical model of Eq. (18).

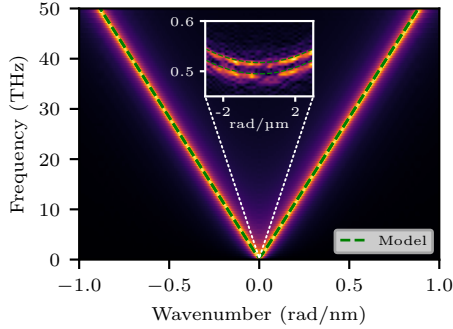


Fig. 3: The simulated dispersion relation is compared with the analytical result in Eq. (18) (green curve). The simulation and material parameters are given in Sec. 4.2. The inset figure is a zoom near the origin, which shows the lifting of the degeneracy due to the external field. To reach the required resolution for this inset, the simulation time was increased to 0.2 ns, the cell length in the direction of the wire to 50 nm and the amount of cells to 5120. In order to clearly show the dispersion relation, the plot only contains the $m_y^{(1)}$ amplitudes and the colors are normalized with respect to the highest amplitude, which is 3.2 for the main figure and 8.7 for the inset.

4.3 Magnetoelastic waves in antiferromagnets

To calculate the dispersion relation of elastic waves, a wave-like ansatz can be inserted in the elastodynamic equation (Eq. (10)):

$$\mathbf{u} = [u_x, u_y, u_z]^T e^{i(\omega t + \mathbf{k} \cdot \mathbf{r})}. \quad (20)$$

To simplify the calculations, we assume an isotropic stiffness tensor, so C_{12} can be replaced by $C_{11} - 2C_{44}$. This was done in Refs. [60, 61], where the authors found three solutions, one of which corresponds to a longitudinal wave and the other two correspond to transversal waves. The dispersion relations are respectively given by

$$\omega_l = \sqrt{C_{11}/\rho} k \quad \text{and} \quad \omega_t = \sqrt{C_{44}/\rho} k. \quad (21)$$

Analogously to Ref. [60], magnetoelastic waves in antiferromagnets are created by coupling the elastodynamic equation (Eq. (10)) to the two sublattice LLG equations (Eq. (1) with (2)), as described in Section 3.3. The elastic waves and spin waves interact, resulting in the anticrossing of the elastic and magnetic dispersion relations [56, 62], creating a characteristic gap.

Building on Section 4.2, we now consider an elastic collinear antiferromagnet, where the uniaxial anisotropy axis, external field and magnetizations still lie in the z -direction. We assume a combined wave-like solution by using Eqs. (16) and (20). The remaining xy -plane isotropy lets us choose the \mathbf{k} -vector in the xz -plane as $\mathbf{k} = k [\sin(\theta), 0, \cos(\theta)]^T$ without loss of generality. The components of the displacement

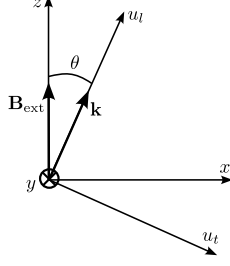


Fig. 4: The different axes as described in Sec. 4.3. The magnetoelastic wave vector \mathbf{k} lies at an angle θ to the external field \mathbf{B}_{ext} and uniaxial anisotropy axis. The latter two lie along the z -axis. The elastic waves have a longitudinal component u_l along \mathbf{k} and an in-plane transversal component u_t perpendicular to \mathbf{k} in the xz -plane. The out-of-plane transversal component u_y lies along the y -axis.

\mathbf{u} in the x - and z - directions are rewritten as components along (u_l) and perpendicular to (u_t) the wave propagation \mathbf{k} . This geometry is illustrated in Fig. 4. Neglecting non-linear terms in the perturbations yields the following set of coupled equations,

$$\begin{aligned}
(\omega^2 - \omega_l^2) \sin(\theta)u_l + (\omega^2 - \omega_{\text{IP}}^2) \cos(\theta)u_t + \frac{iB_2k \cos(\theta)}{\rho} (m_x^{(1)} - m_x^{(2)}) &= 0, \\
(\omega^2 - \omega_{\text{OP}}^2) u_y + \frac{iB_2k \cos(\theta)}{\rho} (m_y^{(1)} - m_y^{(2)}) &= 0, \\
(\omega^2 - \omega_l^2) \cos(\theta)u_l - (\omega^2 - \omega_{\text{IP}}^2) \sin(\theta)u_t + \frac{iB_2k \sin(\theta)}{\rho} (m_x^{(1)} - m_x^{(2)}) &= 0, \\
i\gamma \frac{B_2}{M_S} k \cos(\theta)u_y + i\omega m_x^{(1)} + (\omega_{\text{ext}} + \omega_b)m_y^{(1)} - (\omega_0 - \omega_{12})m_y^{(2)} &= 0, \\
-i\gamma \frac{B_2}{M_S} k[\sin(2\theta)u_l + \cos(2\theta)u_t] + i\omega m_y^{(1)} - (\omega_{\text{ext}} + \omega_b)m_x^{(1)} + (\omega_0 - \omega_{12})m_x^{(2)} &= 0, \\
i\gamma \frac{B_2}{M_S} k \cos(\theta)u_y + i\omega m_x^{(2)} + (\omega_{\text{ext}} - \omega_b)m_y^{(2)} + (\omega_0 - \omega_{12})m_y^{(1)} &= 0, \\
-i\gamma \frac{B_2}{M_S} k[\sin(2\theta)u_l + \cos(2\theta)u_t] + i\omega m_y^{(2)} - (\omega_{\text{ext}} - \omega_b)m_x^{(2)} - (\omega_0 - \omega_{12})m_x^{(1)} &= 0,
\end{aligned}$$

where we defined $\omega_b = \omega_{\text{ani}} - \omega_0 + \omega_{11}$ and used the definitions of ω_{ani} , ω_0 , ω_{11} from Sec. 4.2. The frequencies ω_{IP} and ω_{OP} are the angular frequencies of the in-plane (u_t) and out-of-plane (u_y) polarized transversal elastic waves, respectively. Both are equal to ω_t due to the isotropic stiffness, but are kept separate for interpretation. Writing this in matrix notation using a 7×7 matrix and setting the determinant equal to zero

results in the implicit magnetoelastic dispersion relation:

$$\begin{aligned}
& 2J_{\text{mel}}k^2\omega_{\text{ag}}\cos^2(\theta)\left[J_{\text{mel}}k^2\omega_{\text{ag}}(\omega_l^2+\omega_{\text{IP}}^2-2\omega^2)\right. \\
& \quad -(\omega_l^2-\omega^2)(\omega_{\text{IP}}^2-\omega^2)[\omega_{\text{mag}}^2-\omega_{\text{ext}}^2-\omega^2] \\
& \quad \left.+J_{\text{mel}}k^2\omega_{\text{ag}}(\omega_l^2-\omega_{\text{IP}}^2)\cos(4\theta)\right] \\
& +(\omega_{\text{OP}}^2-\omega^2)\left[-J_{\text{mel}}k^2\omega_{\text{ag}}(\omega_l^2+\omega_{\text{IP}}^2-2\omega^2)[\omega_{\text{mag}}^2-\omega_{\text{ext}}^2-\omega^2]\right. \\
& \quad +(\omega_l^2-\omega^2)(\omega_{\text{IP}}^2-\omega^2)[\omega_{\text{mag}}^2-(\omega_{\text{ext}}-\omega)^2][\omega_{\text{mag}}^2-(\omega_{\text{ext}}+\omega)^2] \\
& \quad \left.-J_{\text{mel}}k^2\omega_{\text{ag}}(\omega_l^2-\omega_{\text{IP}}^2)[\omega_{\text{mag}}^2-\omega_{\text{ext}}^2-\omega^2]\cos(4\theta)\right] \\
& = 0.
\end{aligned} \tag{22}$$

Here we introduced $J_{\text{mel}} = \gamma B_2^2 / \rho M_S$ and

$$\omega_{\text{mag}}^2 = \omega_m \omega_{\text{ag}} = (\omega_{\text{ani}} + \omega_{11} - \omega_{12})(\omega_{\text{ani}} + \omega_{11} + \omega_{12} - 2\omega_0).$$

In mumax⁺ we simulate a one-dimensional wire consisting of 4096 cubic cells of 1 nm³ with periodic boundary conditions in the direction of the wire. The used parameters are based on MnPS₃, with $M_S = 566$ kA/m [46], $a = 0.61$ nm, $K_{u1} = 611$ kJ/m³ [63], $A_{11} = 2.48$ pJ/m, $A_0/a^2 = -0.993$ MJ/m³ and $A_{12} = 0$ J/m [46]. The elastic parameters are chosen to be $\rho = 2800$ kg/m³ [64], $C_{11} = 200$ GPa, $C_{44} = 70$ GPa [63] and $B_1 = B_2 = -5.5$ MJ/m³ [60, 63]. The wave propagation has an angle θ of 30° with respect to the static external field, which has a magnitude of 2 T. This is found to be sufficiently weak to avoid the spin-flop transition, but strong enough to clearly lift the degeneracy. We simulate 0.8 ns while a magnetic field sinc pulse and an external force sinc pulse are applied in every direction. A Fourier transform is then performed on the space- and time-dependent magnetization and displacement components. The result of this simulation can be seen in Fig. 5 alongside the analytical solutions of the uncoupled spin waves (Eq. (18)), elastic waves (Eq. (21)) and the coupled magnetoelastic waves (Eq. (22)).

Fig. 5 shows that the results obtained with mumax⁺ are consistent with the theory. There is clear anticrossing behavior at multiple points, showing the correct interaction between the elastic and spin waves. Even the lifting of the degeneracy between the in-plane (ω_{IP}) and out-of-plane (ω_{OP}) polarized transversal elastic waves (single dotted line in Fig. 5) can be seen in both the analytical result (two dashed lines) and the simulated result (two faintly colored lines).

In the case of wave propagation perpendicular to the magnetization and along the direction of the wire ($\theta = 90^\circ$ in Fig. 4), the out-of-plane polarized and longitudinal elastic waves are uncoupled, while the in-plane polarized waves remain coupled to the

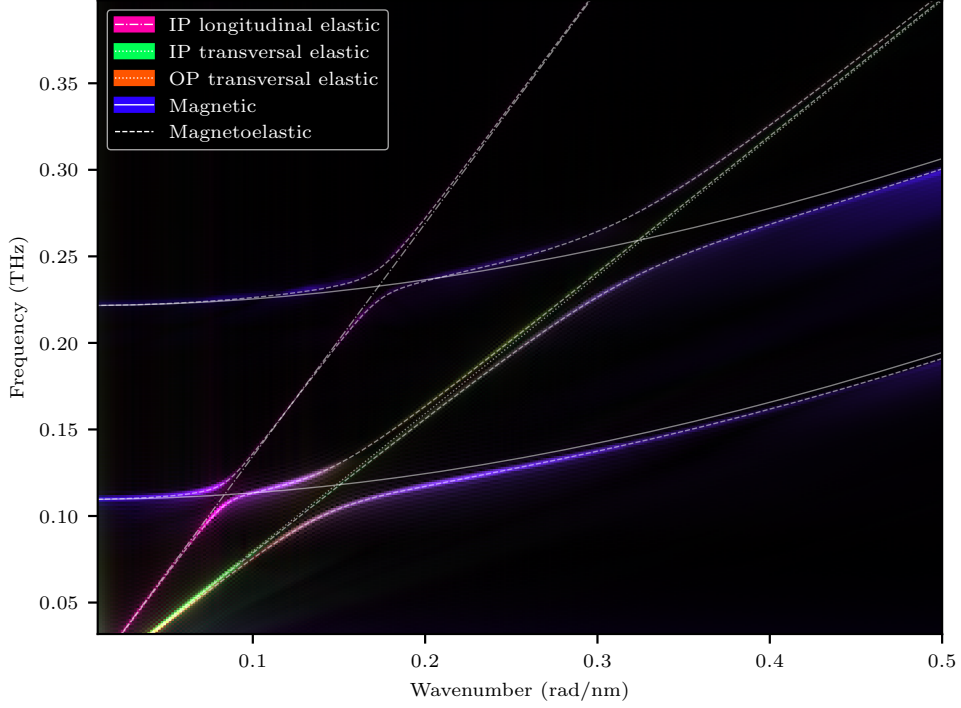


Fig. 5: The dispersion relation for magnetoelastic waves in antiferromagnets. The simulation and material parameters are given in Sec. 4.3 and the angle θ between the direction of wave propagation and the external field is 30° as shown in Fig. 4. A color map is created in arbitrary units by assigning magenta, green, orange and blue to the maximum amplitudes of u_l , u_t , u_y and $m_y^{(1)}$ respectively, all normalized with respect to the highest amplitude. These colors are added together to show the complete dispersion relation. The dash-dotted and dotted curves depict the uncoupled longitudinal elastic and transversal elastic dispersion relations (Eq. (21)) and the solid lines represent the uncoupled spin wave dispersion relations (Eq. (18)). The analytical solution of the coupled dispersion relation (Eq. (22)) is shown by the dashed lines.

spin waves. This can be seen by simplifying Eq. (22), which results in

$$\begin{aligned}
 & (\omega_l^2 - \omega^2)(\omega_{\text{OP}}^2 - \omega^2) \left[-2J_{\text{mel}}k^2\omega_{\text{ag}}(\omega_{\text{mag}}^2 - \omega_{\text{ext}}^2 - \omega^2) \right. \\
 & \left. + (\omega_{\text{IP}}^2 - \omega^2)[\omega_{\text{mag}}^2 - (\omega_{\text{ext}} - \omega)^2][\omega_{\text{mag}}^2 - (\omega_{\text{ext}} + \omega)^2] \right] = 0.
 \end{aligned} \tag{23}$$

This equation is split into three factors and yields three independent solutions. The first two factors lead to the elastic dispersion relations $\omega = \omega_l$ and $\omega = \omega_{\text{OP}}$, which means that the longitudinal and transverse out-of-plane waves are uncoupled. This is also shown in the simulation results shown in Fig. 6, where the anticrossing is only

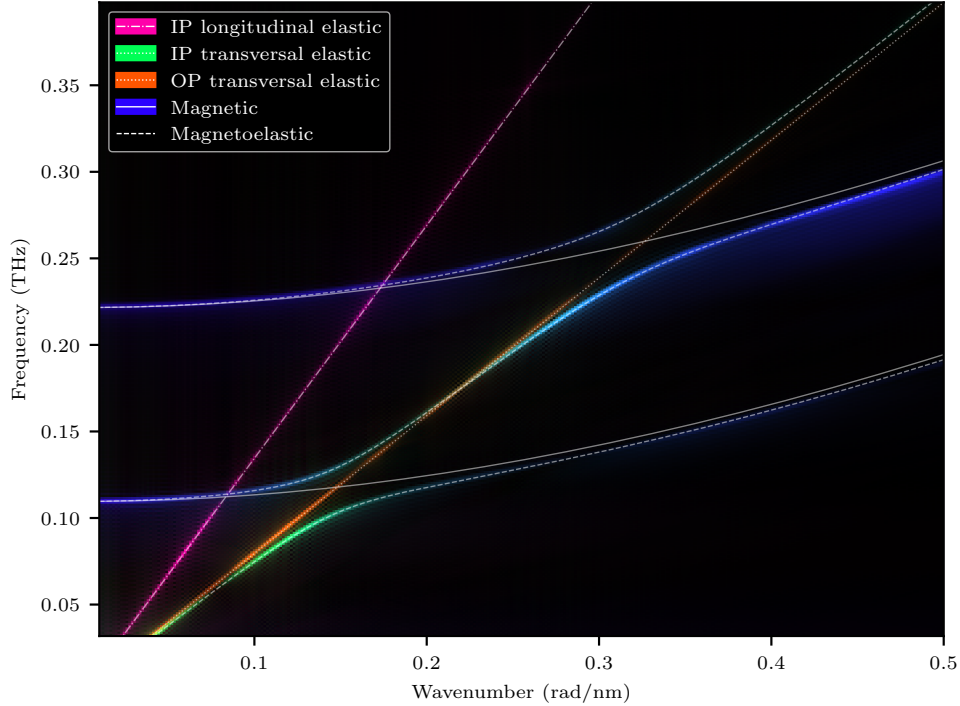


Fig. 6: The dispersion relation for magnetoelastic waves in antiferromagnets for $\theta = 90^\circ$. The simulation parameters and colors are the same as in Fig. 5.

observed between the spin waves and one of the transversal elastic waves, while the other elastic wave dispersion relations remain unchanged. These results qualitatively correspond well to the theoretical results for small wave numbers obtained in Refs. [63, 65].

5 Conclusions and outlook

We presented the micromagnetic model implemented in mumax⁺ and highlighted the key differences from its predecessor mumax³. These advancements include a Python-based interface, support for calculations involving antiferromagnets and ferrimagnets, and the integration of magnetoelasticity across all magnet types in the package.

The correctness of the implementation of antiferromagnetic exchange interactions has been demonstrated in magnetostatics by successfully reproducing the theoretically predicted domain wall width. In dynamic scenarios, the domain wall exhibits the expected velocity when a Slonczewski spin transfer torque is applied. Furthermore, the dispersion relation for spin waves in antiferromagnets has been theoretically derived

and numerically corroborated. Finally, the combination of antiferromagnets with elasticity enables the modeling of magnetoelastic waves with clear anticrossing effects, which mumax⁺ reproduces very well.

The development of mumax⁺ is ongoing and more functionalities are expected to be added in future releases. Some possibilities include non-collinear antiferromagnets, adaptive time stepping appropriate for magnetoelastic simulations, a more general stiffness tensor and piezoelectric coupling. Since mumax⁺ is open-source and built with an object-oriented design for easy extensibility, anyone can, in principle, fork the repository (<https://github.com/mumax/plus>) and enhance the module with additional features.

Acknowledgments

We acknowledge financial support from the SHAPeMe project (EOS ID 400077525) from the FWO and F.R.S.-FNRS under the Excellence of Science (EOS) program.

J.L. was supported by the Fonds Wetenschappelijk Onderzoek (FWO-Vlaanderen) with postdoctoral fellowship No. 12W7622N.

We would like to thank Oleh Kozynets for his software engineering additions to the code.

References

- [1] Donahue, M.: OOMMF User's Guide, Version 1.0. - 6376, National Institute of Standards and Technology, Gaithersburg, MD (1999). <https://doi.org/10.6028/NIST.IR.6376>
- [2] Vansteenkiste, A., Van de Wiele, B.: MuMax: A new high-performance micromagnetic simulation tool. *Journal of Magnetism and Magnetic Materials* **323**(21), 2585–2591 (2011) <https://doi.org/10.1016/j.jmmm.2011.05.037>
- [3] Vansteenkiste, A., Van de Wiele, B., Dvornik, M., Lassalle-Balier, R., Rowlands, G.: mumax2 (2012). <https://github.com/mumax/2>
- [4] Scholz, W., Fidler, J., Schrefl, T., Suess, D., Dittrich, R., Forster, H., Tsiantos, V.: Scalable parallel micromagnetic solvers for magnetic nanostructures. *Computational Materials Science* **28**(2), 366–383 (2003) [https://doi.org/10.1016/S0927-0256\(03\)00119-8](https://doi.org/10.1016/S0927-0256(03)00119-8). Proceedings of the Symposium on Software Development for Process and Materials Design
- [5] Vansteenkiste, A., Leliaert, J., Dvornik, M., Helsen, M., Garcia-Sanchez, F., Van Waeyenberge, B.: The design and verification of MuMax3. *AIP Advances* **4**(10), 107133 (2014) <https://doi.org/10.1063/1.4899186>
- [6] Fischbacher, T., Franchin, M., Bordignon, G., Fangohr, H.: A systematic approach to multiphysics extensions of finite-element-based micromagnetic simulations:

- Nmag. *IEEE Transactions on Magnetics* **43**(6), 2896–2898 (2007) <https://doi.org/10.1109/TMAG.2007.893843>
- [7] MicroMagnetics Team: Magnum.FE: Finite-Element Micromagnetic Simulation. <https://github.com/micromagnetics/magnum.fe>. Accessed: 2024-12-04 (2024)
- [8] Chang, R., Li, S., Lubarda, M.V., Livshitz, B., Lomakin, V.: FastMag: Fast micromagnetic simulator for complex magnetic structures (invited). *Journal of Applied Physics* **109**(7), 07–358 (2011) <https://doi.org/10.1063/1.3563081>
- [9] Kakay, A., Westphal, E., Hertel, R.: Speedup of FEM Micromagnetic Simulations With Graphical Processing Units. *IEEE Transactions on Magnetics* **46**(6), 2303–2306 (2010) <https://doi.org/10.1109/TMAG.2010.2048016>
- [10] Lepadatu, S.: Boris computational spintronics—High performance multi-mesh magnetic and spin transport modeling software. *Journal of Applied Physics* **128**(24), 243902 (2020) <https://doi.org/10.1063/5.0024382>
- [11] Drews, A., Selke, G., Krueger, B., Abert, C., Gerhardt, T.: MicroMagnum: Micromagnetic Simulation Framework. <https://github.com/MicroMagnum/MicroMagnum>. Accessed: 2024-12-04 (2024)
- [12] MicroMagnum Team: Magnum.FD: Finite-Difference Micromagnetic Simulation. <https://github.com/micromagnetics/magnum.fd>. Forked from MicroMagnum, Accessed: 2024-12-04 (2024)
- [13] Baltz, V., Manchon, A., Tsoi, M., Moriyama, T., Ono, T., Tserkovnyak, Y.: Antiferromagnetic spintronics. *Rev. Mod. Phys.* **90**, 015005 (2018) <https://doi.org/10.1103/RevModPhys.90.015005>
- [14] Geim, A.K., Grigorieva, I.V.: Van der Waals heterostructures. *Nature* **499**(7459), 419–425 (2013) <https://doi.org/10.1038/nature12385> . Publisher: Nature Publishing Group. Accessed 2024-12-02
- [15] Bandyopadhyay, S.: Perspective: There is plenty of room for magnetic straintronics in the analog domain. *npj Spintronics* **2**(1), 1–15 (2024) <https://doi.org/10.1038/s44306-024-00018-3> . Publisher: Nature Publishing Group. Accessed 2024-12-02
- [16] Bandyopadhyay, S., Atulasimha, J., Barman, A.: Magnetic straintronics: Manipulating the magnetization of magnetostrictive nanomagnets with strain for energy-efficient applications. *Applied Physics Reviews* **8**(4), 041323 (2021) <https://doi.org/10.1063/5.0062993> . Accessed 2024-12-05
- [17] Van Rossum, G., Drake, F.L.: *Python 3 Reference Manual*. CreateSpace, Scotts Valley, CA (2009)

- [18] Harris, C.R., Millman, K.J., Walt, S.J., Gommers, R., Virtanen, P., Cournapeau, D., Wieser, E., Taylor, J., Berg, S., Smith, N.J., Kern, R., Picus, M., Hoyer, S., Kerkwijk, M.H., Brett, M., Haldane, A., Río, J.F., Wiebe, M., Peterson, P., Gérard-Marchant, P., Sheppard, K., Reddy, T., Weckesser, W., Abbasi, H., Gohlke, C., Oliphant, T.E.: Array programming with NumPy. *Nature* **585**(7825), 357–362 (2020) <https://doi.org/10.1038/s41586-020-2649-2>
- [19] Virtanen, P., Gommers, R., Oliphant, T.E., Haberland, M., Reddy, T., Cournapeau, D., Burovski, E., Peterson, P., Weckesser, W., Bright, J., van der Walt, S.J., Brett, M., Wilson, J., Millman, K.J., Mayorov, N., Nelson, A.R.J., Jones, E., Kern, R., Larson, E., Carey, C.J., Polat, İ., Feng, Y., Moore, E.W., VanderPlas, J., Laxalde, D., Perktold, J., Cimrman, R., Henriksen, I., Quintero, E.A., Harris, C.R., Archibald, A.M., Ribeiro, A.H., Pedregosa, F., van Mulbregt, P., SciPy 1.0 Contributors: SciPy 1.0: Fundamental Algorithms for Scientific Computing in Python. *Nature Methods* **17**, 261–272 (2020) <https://doi.org/10.1038/s41592-019-0686-2>
- [20] Hunter, J.D.: Matplotlib: A 2d graphics environment. *Computing in Science & Engineering* **9**(3), 90–95 (2007) <https://doi.org/10.1109/MCSE.2007.55>
- [21] ISO/IEC: ISO/IEC 14882:2024 - Programming Languages – C++. ISO/IEC Standard (2020). <https://www.iso.org/standard/83626.html>
- [22] NVIDIA Corporation: NVIDIA CUDA C Programming Guide. Version 12.6 (2024)
- [23] Joos, J.J., Bassirian, P., Gypens, P., Mulkers, J., Litzius, K., Van Waeyenberge, B., Leliaert, J.: Tutorial: Simulating modern magnetic material systems in mumax3. *Journal of Applied Physics* **134**(17) (2023)
- [24] μ MAG organization: μ MAG Micromagnetic Modeling Activity Group (2021). <https://www.ctcms.nist.gov/~rdm/mumag.org.html> Accessed 2024-11-25
- [25] Foley, J.D.: *Computer Graphics: Principles and Practice*. Addison-Wesley systems programming series. Addison-Wesley, Boston (1996)
- [26] Zhang, S., Li, Z.: Roles of Nonequilibrium Conduction Electrons on the Magnetization Dynamics of Ferromagnets. *Phys. Rev. Lett.* **93**, 127204 (2004) <https://doi.org/10.1103/PhysRevLett.93.127204>
- [27] Slonczewski, J.C.: Current-driven excitation of magnetic multilayers. *Journal of Magnetism and Magnetic Materials* **159**(1), 1–7 (1996) [https://doi.org/10.1016/0304-8853\(96\)00062-5](https://doi.org/10.1016/0304-8853(96)00062-5)
- [28] Landau, L., Lifshitz, E.: On the theory of the dispersion of magnetic permeability in ferromagnetic bodies. reproduced in collected papers of ld landau. Pergamon, New York (1935)

- [29] Gilbert, T.L.: A Lagrangian formulation of the gyromagnetic equation of the magnetization field. *Phys. Rev.* **100**, 1243 (1955)
- [30] Leliaert, J., Mulkers, J., De Clercq, J., Coene, A., Dvornik, M., Van Waeyenberge, B.: Adaptively time stepping the stochastic Landau-Lifshitz-Gilbert equation at nonzero temperature: Implementation and validation in MuMax3. *AIP Advances* **7**(12), 125010 (2017) <https://doi.org/10.1063/1.5003957>
- [31] Sánchez-Tejerina, L., Puliafito, V., Khalili Amiri, P., Carpentieri, M., Finocchio, G.: Dynamics of domain-wall motion driven by spin-orbit torque in antiferromagnets. *Phys. Rev. B* **101**, 014433 (2020) <https://doi.org/10.1103/PhysRevB.101.014433>
- [32] Newell, A.J., Williams, W., Dunlop, D.J.: A generalization of the demagnetizing tensor for nonuniform magnetization. *Journal of Geophysical Research: Solid Earth* **98**(B6), 9551–9555 (1993) <https://doi.org/10.1029/93JB00694>
- [33] Press, W.H.: *Numerical Recipes 3rd Edition: The Art of Scientific Computing*. Numerical Recipes: The Art of Scientific Computing. Cambridge University Press, Cambridge (2007)
- [34] Lopez-Diaz, L., Aurelio, D., Torres, L., Martinez, E., Hernandez-Lopez, M.A., Gomez, J., Alejos, O., Carpentieri, M., Finocchio, G., Consolo, G.: Micromagnetic simulations using Graphics Processing Units. *Journal of Physics D: Applied Physics* **45**(32), 323001 (2012) <https://doi.org/10.1088/0022-3727/45/32/323001>
- [35] Chernyshenko, D., Fangohr, H.: Computing the demagnetizing tensor for finite difference micromagnetic simulations via numerical integration. *Journal of Magnetism and Magnetic Materials* **381**, 440–445 (2015) <https://doi.org/10.1016/j.jmmm.2015.01.013>
- [36] Hals, K.M.D., Everschor-Sitte, K.: New Boundary-Driven Twist States in Systems with Broken Spatial Inversion Symmetry. *Phys. Rev. Lett.* **119**, 127203 (2017) <https://doi.org/10.1103/PhysRevLett.119.127203>
- [37] Mahfouzi, F., Kioussis, N.: Bulk generalized Dzyaloshinskii-Moriya interaction in \mathcal{PT} -symmetric antiferromagnets. *Phys. Rev. B* **106**, 220404 (2022) <https://doi.org/10.1103/PhysRevB.106.L220404>
- [38] Breth, L., Suess, D., Vogler, C., Bergmair, B., Fuger, M., Heer, R., Brueckl, H.: Thermal switching field distribution of a single domain particle for field-dependent attempt frequency. *Journal of Applied Physics* **112**(2), 023903 (2012) <https://doi.org/10.1063/1.4737413>
- [39] Graff, K.F.: *Wave Motion in Elastic Solids*. (1975)
- [40] Achenbach, J.D.: *Wave Propagation in Elastic Solids*. North-Holland Publishing

Company/American Elsevier, Amsterdam (1973)

- [41] Sadd, M.H.: Elasticity: Theory, Applications, and Numerics. Academic Press, London (2009)
- [42] Vanderveken, F., Mulkers, J., Leliaert, J., Van Waeyenberge, B., Sorée, B., Zografos, O., Zografos, O., Ciubotaru, F., Adelman, C.: Finite difference magnetoelastic simulator. *Open Research Europe* **1**(35) (2021) <https://doi.org/10.12688/openreseurope.13302.1>
- [43] Barber, J.R.: Elasticity. Solid Mechanics and Its Applications. Springer, Dordrecht (2012)
- [44] Sauer, T., Sauer, T.: Numerical Analysis. Always learning. Pearson, London (2012)
- [45] Chikazumi, S.: Physics of Ferromagnetism. International Series of Monographs on Physics. OUP Oxford, Oxford (2009)
- [46] Barra, A., Domann, J., Kim, K.W., Carman, G.: Voltage Control of Antiferromagnetic Phases at Near-Terahertz Frequencies. *Phys. Rev. Appl.* **9**, 034017 (2018) <https://doi.org/10.1103/PhysRevApplied.9.034017>
- [47] Leader, J.J.: Numerical Analysis and Scientific Computation. Pearson Addison Wesley, Edinburgh (2004). <https://books.google.be/books?id=y-XEGAAACAAJ>
- [48] Bogacki, P., Shampine, L.F.: A 3(2) pair of runge - kutta formulas. *Applied Mathematics Letters* **2**(4), 321–325 (1989) [https://doi.org/10.1016/0893-9659\(89\)90079-7](https://doi.org/10.1016/0893-9659(89)90079-7)
- [49] Cash, J.R., Karp, A.H.: A variable order runge-kutta method for initial value problems with rapidly varying right-hand sides. *ACM Trans. Math. Softw.* **16**(3), 201–222 (1990) <https://doi.org/10.1145/79505.79507>
- [50] Fehlberg, E., Center, G.C.M.S.F.: Low-order Classical Runge-Kutta Formulas with Stepsize Control and Their Application to Some Heat Transfer Problems. NASA technical report. National Aeronautics and Space Administration, Washington (1969)
- [51] Dormand, J.R., Prince, P.J.: A family of embedded runge-kutta formulae. *Journal of Computational and Applied Mathematics* **6**(1), 19–26 (1980) [https://doi.org/10.1016/0771-050X\(80\)90013-3](https://doi.org/10.1016/0771-050X(80)90013-3)
- [52] Exl, L., Bance, S., Reichel, F., Schrefl, T., Peter Stimming, H., Mauser, N.J.: LaBonte’s method revisited: An effective steepest descent method for micromagnetic energy minimization. *Journal of Applied Physics* **115**(17), 17–118 (2014) <https://doi.org/10.1063/1.4862839>

- [53] Krekel, H., Oliveira, B., Pfannschmidt, R., Bruynooghe, F., Laughner, B., Bruhin, F.: pytest (2004). <https://github.com/pytest-dev/pytest>
- [54] Cottam, M.G.: Linear and Nonlinear Spin Waves in Magnetic Films and Superlattices. WORLD SCIENTIFIC, New Jersey (1994). <https://doi.org/10.1142/1687>
- [55] Stancil, D.D., Prabhakar, A.: Spin Waves: Theory and Applications. Springer, New York (2009)
- [56] Gurevich, A.G., Melkov, G.A.: Magnetization Oscillations and Waves. Taylor & Francis, London (1996)
- [57] Coey, J.M.D.: Magnetism and Magnetic Materials. Magnetism and Magnetic Materials. Cambridge University Press, Cambridge (2010)
- [58] Samuelsen, E.J., Shirane, G.: Inelastic neutron scattering investigation of spin waves and magnetic interactions in α -Fe₂O₃. *physica status solidi (b)* **42**(1), 241–256 (1970) <https://doi.org/10.1002/pssb.19700420125>
- [59] Samuelsen, E.J., Hutchings, M.T., Shirane, G.: Inelastic neutron scattering investigation of spin waves and magnetic interactions in Cr₂O₃. *Physica* **48**(1), 13–42 (1970) [https://doi.org/10.1016/0031-8914\(70\)90158-8](https://doi.org/10.1016/0031-8914(70)90158-8)
- [60] Vanderveken, F., Ciubotaru, F., Adelman, C.: In: Kamenetskii, E. (ed.) *Magnetoelastic Waves in Thin Films*, pp. 287–322. Springer, Cham (2021). https://doi.org/10.1007/978-3-030-62844-4_12
- [61] Achenbach, J.D.: *Wave Propagation in Elastic Solids*. Applied Mathematics and Mechanics Series. North-Holland Publishing Company, Amsterdam (1973)
- [62] Tucker, J.W., Rampton, V.W.: *Microwave Ultrasonics in Solid State Physics*. Amsterdam : North-Holland, Amsterdam (1972)
- [63] Zhang, S., Go, G., Lee, K.-J., Kim, S.K.: SU(3) Topology of Magnon-Phonon Hybridization in 2D Antiferromagnets. *Phys. Rev. Lett.* **124**, 147204 (2020) <https://doi.org/10.1103/PhysRevLett.124.147204>
- [64] Jain, A., Ong, S., Hautier, G., Chen, W., Richards, W., Dacek, S., Cholia, S., Gunter, D., Skinner, D., Ceder, G., Persson, K.: Commentary: The Materials Project: A materials genome approach to accelerating materials innovation. *APL Materials* **1**, 011002 (2013) <https://doi.org/10.1063/1.4812323>
- [65] Go, G., Yang, H., Park, J.-G., Kim, S.K.: Topological magnon polarons in honeycomb antiferromagnets with spin-flop transition. *Phys. Rev. B* **109**, 184435 (2024) <https://doi.org/10.1103/PhysRevB.109.184435>